Soft Matter

ARTICLE TYPE

Cite this: DOI: 00.0000/xxxxxxxxxx

Lipid Vesicles Induced Ordered Nanoassemblies of Janus Nanoparticles†

Yu Zhu,[a] Abash Sharma,[a] Eric J. Spangler,[a] Jan-Michael Y. Carrillo,[b] P.B. Sunil Kumar[c] and Mohamed Laradji[a*]

Received Date
Accepted Date

DOI: 00.0000/xxxxxxxxxx

Since many advanced applications require specific assemblies of nanoparticles (NPs), considerable efforts have been made to fabricate nanoassemblies with specific geometries. Although nanoassemblies can be fabricated through top-down approaches, recent advances show that intricate nanoassemblies can also be obtained through guided self-assembly, mediated for example by DNA strands. Here, we show, through extensive molecular dynamics simulations, that highly ordered self-assemblies of NPs can be mediated by their adhesion to lipid vesicles (LVs). Specifically, Janus NPs are considered so that the amount by which they are wrapped by the LV is controlled. The specific geometry of the nanoassembly is the result of effective curvature-mediated repulsion between the NPs and the number of NPs adhering to the LV. The NPs are arranged on the LV into polyhedra which satisfy the upper limit of Euler's polyhedral formula, including several deltahedra and three Platonic solids, corresponding to the tetrahedron, octahedron, and icosahedron.

1 Introduction

Intricate assemblies of nanoparticles (NPs) can potentially be used in many advanced applications, including data storage[1], light harvesting[2], non-linear optics[3], catalysis[4] and biosensing[5]. The advantage of NPs assemblies or superlattices, over dilute NPs dispersions, stems from novel collective phenomena arising from NPs proximity and increased net surface area per volume of the nanomaterial. For example, close proximity of Au or Ag NPs leads to coupling between their surface plasmons and enhancement of the electromagnetic field in the gaps between them. This results in useful phenomena, including surface-enhanced Raman scattering[6] and plasmon-enhanced luminescence[7]. These can be exploited for numerous applications such as ultra-sensitive biosensing and imaging[8–10].

Properties of NPs clusters can be controlled through careful design of the NPs geometry, chemistry, and structure of their nanoassembly. Considerable efforts have therefore been made to fabricate nanoassemblies with specific geometries. Nanoassemblies fabrication is achieved through either top-down approaches, such as laser machining[11] and a variety of lithography techniques[12], or bottom-up approaches which rely on NPs self-assembly. The latter is typically mediated by macromolecules including copolymers[13], DNA[14,15], proteins[16,17], and cellulose[18]. Various nanoassemblies, including dimers[19], trimers[20], tetramers[21], icosamers[22], pyramids[23], tori[24], and chiral structures[25], have been synthesized through bottom-up approaches.

It is well established that, due to their flexibility, lipid membranes (LMs) induce interactions between adhering NPs, which can result in their self-assembly[26–33]. Unfortunately, the potential of planar LMs or lipid vesicles (LVs) to self-assemble uniform NPs is limited by the fact that these aggregates are linear in-plane or tubular chains, in which neighbouring NPs are practically in contact with each other[26,29–31]. The ability of planar LMs or large LVs to aggregate NPs with uniform surfaces requires an appreciable degree of wrapping of the NPs by the membrane, which is satisfied when the excess bending energy, $8\pi\kappa$, where κ is the bending modulus, is about the adhesive energy, $\xi\pi D_{NP}^2$, where D_{NP} is the NPs diameter and ξ is the adhesive interaction per unit of area. Consequently, LMs are only able to self-assemble NPs with uniform surfaces over a narrow range of values of ξ and D_{NP} such that $\xi D_{NP}^2 \approx 8\kappa$. For $\xi D_{NP}^2 \ll 8\kappa$, NPs are dispersed on the LM or LV, with positions that are spatially uncorrelated, whereas for $\xi D_{NP}^2 \gg 8\kappa$, the NPs are endocytosed.

The limitations in using LMs as a medium for self-assembling NPs into aggregates over a wide range of parameters, such that the NPs are not in contact with each other, can be overcome by allowing an appreciable degree of wrapping of the NPs by the

[a] Department of Physics and Materials Science, The University of Memphis, Memphis, TN 38152, USA
[b] Center for Nanophase Materials Sciences, Oak Ridge National Laboratory, Oak Ridge, TN 37831, USA
[c] Department of Physics, Indian Institute of Technology Madras, Chennai 600036, India
* mlaradji@memphis.edu

† Electronic Supplementary Information (ESI) available. See DOI: 10.1039/cXsm00000x/

membrane while suppressing their endocytosis. We show in this article that this problem is mitigated by NPs surface modification into Janus NPs (JNPs)[34], such that one moiety has a stronger affinity to the lipid head groups than the solvent, while the other moiety has a stronger affinity to the solvent than the lipids[35–37]. This allows for the self-assembly of the NPs into highly ordered nanoclusters over a wide range of parameters.

2 Model and Numerical Approach

The present study is based on an implicit-solvent model of self-assembled lipid membranes[38,39], in which a lipid molecule is coarse-grained into a short semi-flexible chain composed of one head (h) bead and two tail (t) beads. The potential energy of the lipid bilayer is given by

$$\begin{aligned} U(\{\mathbf{r}_i\}) &= \sum_{i,j} U_0^{\alpha_i\alpha_j}(r_{ij}) + \sum_{\langle i,j\rangle} U_{\text{bond}}^{\alpha_i\alpha_j}(r_{ij}) \\ &+ \sum_{\langle i,j,k\rangle} U_{\text{bend}}^{\alpha_i\alpha_j\alpha_k}(\mathbf{r}_i,\mathbf{r}_j,\mathbf{r}_k), \end{aligned} \tag{1}$$

where $\mathbf{r}_i$ denotes the coordinates of bead i, $r_{ij}=|\mathbf{r}_i-\mathbf{r}_j|$, and $\alpha_i(=h \text{ or } t)$ denotes the type of bead i. The angular bracket in the second summation of Eq. (1) indicates that i and j are bonded within the same lipid chain. Likewise, the angular bracket in the third summation indicates that i, j and k are part of the same lipid chain. In Eq. (1), $U_0^{\alpha\beta}$ is a soft two-body potential, between beads of types α and β and is given by

$$U_0^{\alpha\beta}(r)=\begin{cases} \left(U_{\max}^{\alpha\beta}-U_{\min}^{\alpha\beta}\right)\frac{(r_m-r)^2}{r_m^2}+U_{\min}^{\alpha\beta} & \text{if } r\le r_m, \\ -2\,U_{\min}^{\alpha\beta}\frac{(r_c-r)^3}{(r_c-r_m)^3}+3\,U_{\min}^{\alpha\beta}\frac{(r_c-r)^2}{(r_c-r_m)^2} & \text{if } r_m<r\le r_c, \\ 0 & \text{if } r>r_c, \end{cases}$$

where $U_{\max}^{\alpha\beta}>0$ and $U_{\min}^{\alpha\beta}\le 0$ for any pair (α,β). $U_{\min}^{\alpha\beta}=0$ implies a fully repulsive interaction between α and β, and $U_{\min}^{\alpha\beta}<0$ implies a short-range attraction between the two beads. The self-assembly of the lipids into thermodynamically stable bilayers is ensured by choosing $U_{\min}^{hh}=U_{\min}^{ht}=0$ and strong enough negative value of $U_{\min}^{tt}$[39]. r_m is the size of a bead and r_c is the cutoff distance of the interaction between two tail beads.

In Eq. (1), $U_{\text{bond}}^{\alpha_i\alpha_j}$ ensures connectivity between beads that belong to the same lipid chain and is given by

$$U_{\text{bond}}^{\alpha_i\alpha_j}(r_{ij})=\frac{k_{\text{bond}}^{\alpha_i\alpha_j}}{2}\left(r_{ij}-a_{\alpha_i\alpha_j}\right)^2, \tag{2}$$

where $k_{\text{bond}}^{\alpha_i\alpha_j}$ is the bond stiffness coefficient and $a_{\alpha_i\alpha_j}$ is the preferred bond length between beads i and j of types α_i and α_j, respectively. It is noted that in addition to this bonding interaction, bonded beads within a lipid chain also interact with each other through $U_0^{\alpha_i\alpha_j}$.

Finally, $U_{\text{bend}}^{\alpha\beta\gamma}$ in Eq. (1) is a three-body potential that provides bending stiffness to the lipid chains and is given by

$$U_{\text{bend}}^{\alpha_i\alpha_j\alpha_k}(\mathbf{r}_i,\mathbf{r}_j,\mathbf{r}_k)=\frac{k_{\text{bend}}^{\alpha_i\alpha_j\alpha_k}}{2}\left(\cos\varphi_0-\frac{\mathbf{r}_{ij}\cdot\mathbf{r}_{kj}}{r_{ij}r_{kj}}\right)^2, \tag{3}$$

where k_{bend}^{htt} is the bending stiffness coefficient and φ_0 is the preferred splay angle of the lipid chain, taken to be 180°.

A Janus NP is initially constructed as an icosahedron mesh followed by three subsequent triangulations, resulting into 642 nodes (beads of type n) and 1280 elementary triangles[40]. The nodes are then projected onto a sphere, of diameter D_{NP}, with same center as the original icosahedron. Two neighbouring beads of the NP are connected via the harmonic potential given by Eq. (2) with a bond stiffness k_{bond}^{nn} and a preferred bond length $a_{nn}=l$. To provide further rigidity to the NP, the three-body interaction, given by Eq. (3) with a bending stiffness coefficient k_{bend}^{nnn}, is added to every connected triplet of beads. The preferred bond angle φ_0^{nnn} of each triplet is determined from the initial configuration of the NP.

Since a NP is hollow in this model, the two-body and three-body interactions are found to not be sufficient to provide a very rigid spherical structure of the NP, unless k_{bond}^{nn} and k_{bend}^{nnn} are very high, which is not desirable since this would require very small values of the integration time step. This problem is overcome by introducing a bead of type c, at the center of the NP, which is bonded to all n-beads, of the NP's surface, by a harmonic potential given by Eq. (2) with a bond stiffness k_{bond}^{cn} and a preferred bond length $a_{cn}=D/2$.

A Janus NP is comprised of two types of beads. These correspond to n_a-beads, which interact attractively with the h-beads, and n_b-beads, which interact repulsively with the h-beads. Both n_a- and n_b-beads interact repulsively with t-beads. $U_0^{\alpha_i\alpha_j}$, given by Eq. 2, is used for the interactions between the n_a- and n_b-beads with the h- and t-beads, with $U_{\min}^{n_ah}=\mathscr{E}<0$ and $U_{\min}^{n_bh}=U_{\min}^{n_at}=U_{\min}^{n_bt}=0$. This ensures that only n_a-beads have a tendency to adhere to the membrane. Beads belonging to different NPs interact with each via the same two-body potential $U_0^{\alpha_i\alpha_j}$. This interaction is chosen to be fully repulsive ($U_{\min}^{n_an_a}=U_{\min}^{n_bn_b}=U_{\min}^{n_an_b}=0$) to prevent the NPs from aggregation in the absence of lipid membranes. The term Janusity (J) is introduced to define the area fraction of the NP that interacts attractively with the lipid head groups, i.e. $J=d/D$, where d is the height of the spherical cap that interacts attractively with the lipid head beads. Fig. S1 (ESI†) depicts an equilibrated Janus NP with $J=0.5$.

All beads are moved using a molecular dynamics scheme with a Langevin thermostat[41],

$$\begin{aligned} \dot{\mathbf{r}}_i(t) &= \mathbf{v}_i(t) \\ m\dot{\mathbf{v}}_i(t) &= -\nabla_i U(\{\mathbf{r}_i\})-\Gamma\mathbf{v}_i(t)+\sigma\chi_i(t), \end{aligned} \tag{4}$$

where m is the mass of a bead (same for all beads), Γ is a bead's friction coefficient, and $\sigma\chi_i(t)$ is a random force originating from the heat bath. $\chi_i(t)$ is a random vector generated from a uniform distribution and obeys $\langle\chi_i(t)\rangle=0$ and $\langle\chi_i^{(\mu)}(t)\chi_j^{(\nu)}(t')\rangle=\delta_{\mu\nu}\delta_{ij}\delta(t-t')$, where μ and $\nu=x$, y or z. The dissipative and random forces are interrelated through the dissipation-fluctuation theorem, which leads to $\Gamma=\sigma^2/2k_BT$.

The values of the parameters of the model, are given in Table 1. The interaction parameters of the lipids are chosen such that they spontaneously self-assemble into bilayers and such that the value

Table 1 Model parameters

Parameter	Value
$U^{hh}_{\max}$, $U^{ht}_{\max}$	100ε
$U^{tt}_{\max}$	200ε
$U^{hh}_{\min}$, $U^{ht}_{\min}$	0
$U^{tt}_{\min}$	-6ε
$U^{n_a h}_{\max}$	200ε
$U^{n_a h}_{\min}$	$-\mathscr{E}$
$U^{n_b h}_{\max}$, $U^{n_b t}_{\max}$, $U^{n_a t}_{\max}$	100ε
$U^{n_b h}_{\min}$, $U^{n_b t}_{\min}$, $U^{n_a t}_{\min}$	0
$U^{n_a n_a}_{\max}$, $U^{n_a n_b}_{\max}$, $U^{n_b n_b}_{\max}$	200ε
$U^{n_a n_a}_{\min}$, $U^{n_a n_b}_{\min}$, $U^{n_b n_b}_{\min}$	0
k^{ht}_{bond}, k^{tt}_{bond}	$100\varepsilon/r_m^2$
k^{htt}_{bend}	100ε
k^{nn}_{bond}	1200ε
k^{nn}_{bond}	$1200\varepsilon/r_m^2$
k^{nc}_{bond}	$45\varepsilon/r_m^2$
k^{nnn}_{bend}	250ε
r_c	$2r_m$
a_{ht}, a_{tt}	$0.7r_m$
a_{cn}	$D_{NP}/2$

of the bending modulus of the bare bilayer in the fluid phase is comparable to experimental values[39]. For the particular parameters in Table 1 with $\varepsilon = k_BT/3$, the bending modulus of the bare bilayer, as extracted from the spectrum of the height fluctuations of the bilayer, is $\kappa \approx 30k_BT$[39], which is comparable to that of a DPPC bilayer in the fluid phase[42].

The simulations are performed on LVs with diameter, D_{LV}, ranging between 48 and 125 nm. Here, D_{LV} is defined as twice the average distance between the positions of the h-beads of the outer leaflet and the LV's center of mass. This corresponds to a total number of lipid chains in a LV ranging between 25000 and 170000). The diameter of the NPs is $D_{NP} = 20$ nm. In a typical simulation, n NPs, which are initially placed close to an equilibrated LV at random positions, quickly adhere to the LV. The system is then equilibrated over a large number of steps (typically over at least 2×10^7 time steps), and the results are collected once equilibrium is reached. All simulations are executed at $k_BT = 3.0\varepsilon$, with a time step $\Delta t = 0.02\tau$, where $\tau = r_m(m/\varepsilon)^{1/2}$. Both Eqs. (4) are integrated using the velocity-Verlet algorithm[43] with $\Gamma = \sqrt{6}m/\tau$. By comparing the thickness of this model bilayer in the fluid phase, which is about $4r_m$, with that of a typical fluid phospholipid bilayer, which is about 4 nm, we estimate $r_m \approx 1$ nm. Hence, in the remainder of this article, all lengths are expressed in nanometers, and the adhesion energy density, ξ, is expressed in k_BT/nm^2. The adhesion energy density is defined as $\xi = |U_{adh}|/A_{adh}$, where U_{adh} is the net potential energy between the NP and the membrane and A_{adh} is the area of the NP adhering to the membrane. Details of the calculation of ξ are found in Refs.[37,44] and the relationship between ξ and $\mathscr{E}$ is shown in Fig. S2 (ESI†).

3 Results

To infer whether LVs are able to assemble spherical NPs with uniform surfaces into ordered nanoclusters, in which the NPs are not endocytosed and are apart from each, we performed a series of coarse-grained molecular dynamics simulations based on the model and numerical approach presented in the section Methods. These simulations are performed on $n = 6$, 8 and 10 uniform NPs, with $D_{NP} = 20$ nm adhering to LVs with different diameters, D_{LV}, and at different values of ξ. The resulting ξ-D_{LV} phase diagrams, shown in Figs. 1 (A-C), demonstrate that the NPs adhere to the LVs monomerically (disordered state) at low values of ξ. Within this disordered phase, the positions of the NPs are weakly correlated (see snapshots (a), (c), (f) and (k) in Figs. 1 (A-C)). As ξ is increased, one or more NPs are endocytosed, while the remaining NPs adhering to the main LV are dispersed as monomers (see snapshots (b), (g) and (i) in Fig. 1). In the cases of $n = 8$ and 10, the disordered and endocytosis phases are separated by a phase, spanning a narrow range of values of ξ, in which the NPs aggregate into either in-plane or tubular chains, where the NPs are invaginated into a pocket but not detached from the vesicle, as shown by snapshots (d), (e), (j) and (l) in Figs. 1 (B) and (C). A characteristic of these aggregates is that the NPs within them are in contact with each other, in line with earlier studies[26,29–32].

Correlations in the positions of the NPs on the vesicle in the disordered phase are inferred from the radial distribution function (RDF), shown in Fig. 1 (D) for the case of $n = 6$ at $D_{LV}/D_{NP} = 3.4$. This figure shows that with increasing ξ, two broad peaks emerge in the RDF. This implies that the increase in ξ, which leads to the increase in the degree of wrapping of the NPs by the LV as shown by the inset of Fig. 1 (D), promotes correlations in the NPs positions. The breadth of the RDF peaks, and the snapshots (a), (c), (f) and (k) in Fig. 1, clearly show that the NPs placement on the LV remains disordered. This confirms many earlier studies[26,29–32]. Nonetheless, snapshot (a) demonstrates that the configuration of the vesicle for $n = 6$ is a deformed cube with the NPs around the centers of its faces. This concurs with the fact that the ratio between the positions of the second and first peaks of the RDF at $\xi = 1.47k_BT/\text{nm}^2$ is close to $\sqrt{2}$. In contrast, the NPs in snapshots (c), (f) and (k) which are also very close to the transition from the disordered to the endocytosis or chain/tube phase, are clearly more disordered than in (a). This indicates that the degree of NPs positional correlations decreases with increasing D_{LV} or n. This is also demonstrated by the RDFs corresponding to these configurations shown in Fig. S3 (ESI†).

The trend of the RDFs, shown in Fig. 1 (D), suggests that highly ordered NPs nanoclusters, in which the NPs are apart, can be achieved if the degree of wrapping of individual NPs is high and at the same time endocytosis is suppressed. This can be achieved by surface modification of the NPs to Janus NPs (JNPs)[34] to control their degree of wrapping. Namely, one moiety (of area fraction J) of the NP is modified such that it has a higher affinity to the lipid head groups than the solvent, while the other moiety has a

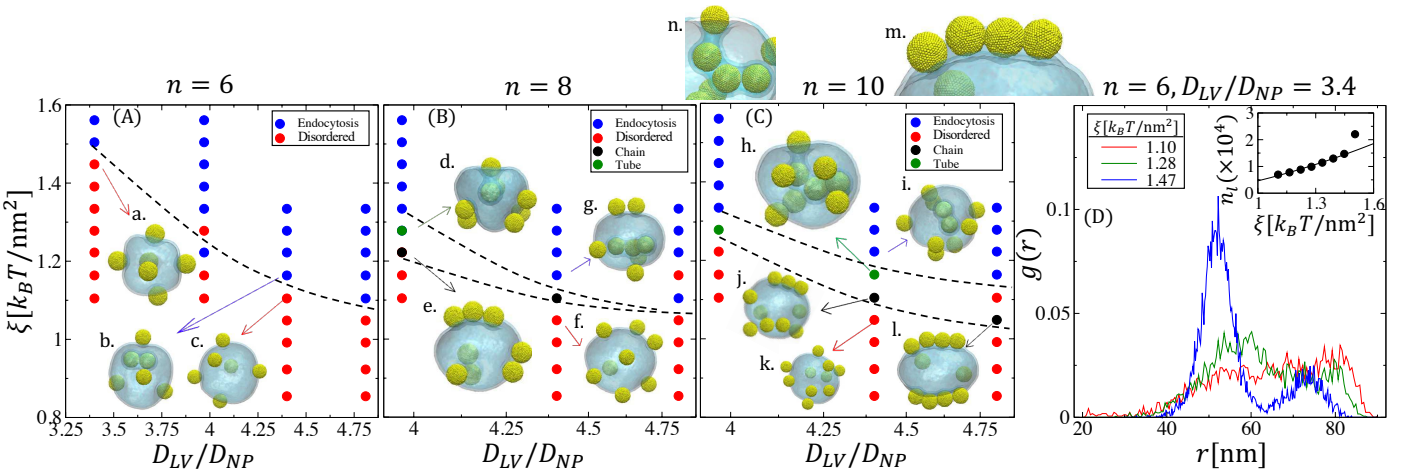

Fig. 1 Phase diagram of the adhesion modes of n uniform spherical NPs ($J = 1$) in terms of the ratio D_{LV}/D_{NP} and adhesion strength ξ. (A), (B) and (C) correspond to $n = 6$, 8 and 10, respectively. Red symbols correspond to states where the NPs adhere to the vesicle in the disordered state. Blue symbols correspond to states where the vesicle undergoes a topological change with at least one endocytosed NP. Black and green symbols correspond to states where NPs cluster into in-plane linear chains (including dimers) or tubular chains. Snapshots (a-l) are at equilibrium. Snapshot (m) shows a self-assembled in-plane linear chain from snapshot (l). Snapshot (n) shows a self-assembled tubular chain from snapshot (h). (D) Radial distribution function, $g(r)$, of the NPs centers of mass at three values of ξ within the disordered phase for the case of $n = 6$ and $D_{LV}/D_{NP} = 3.4$. Inset of (D) shows the number of lipid head beads, interacting with the NPs, vs ξ for the same system. The last point in the inset is in the endocytosis phase.

higher affinity to the solvent[35–37]. A large number of simulations are then carried with JNPs with $J = 0.5$ and $\xi = 4.11\,k_BT/\text{nm}^2$. This value of ξ is high enough to ensure that the JNP moiety, with affinity to the lipid head groups, is wrapped by the membrane as much as possible[37].

Different views of equilibrium configurations of LVs with $3 \leq n \leq 14$ are shown by the top two rows of Fig. 2. Here, the value of D_{LV} is such that the LV's surface area per JNP is 2453 nm^2 (see Fig. S4 (ESI†)). These snapshots indicate that although the adhering JNPs on the LVs are apart, they are self-assembled into surprisingly ordered nanoclusters with geometries dependent on n. These nanoassemblies are fundamentally different from those of NPs with uniform surfaces, shown in Fig. 1. Formation of these nanoclusters is shown for different values of n in Movies 1 to 8 in ESI†. These movies also provide different views of the nanoclusters.

Figure 2 shows that 3 JNPs form an equilateral triangle and that the cross-section of the LV along the plane containing the JNPs centers is also an equilateral triangle. The first two rows of Fig. 2, for $n > 3$, show LVs that are fairly faceted into highly symmetric polyhedra, shown schematically in the third row. Here, the polyhedra edges (blue segments) correspond to highly bent regions of the membrane, and JNPs are represented by red beads. Particularly interesting configurations in Fig. 2 are the three Platonic solids, namely regular tetrahedron, cube and dodecahedron for $n = 4$, 6 and 12, respectively.

The fourth row of Fig. 2 depicts polyhedra whose vertices (red beads) correspond to time-averaged positions of the JNPs at equilibrium, and whose edges (blue segments) are links connecting each JNP to its nearest neighbours, obtained using spherical Delaunay triangulation[45]. These polyhedra are strictly convex and dual to the LVs polyhedra, which is expected since the JNPs are located around the centers of the faces of the LVs polyhedra. Consequently, the nanoclusters for $n = 4$, 6 and 12 are also Platonic solids, corresponding respectively to the tetrahedron, octahedron and icosahedron. The fourth row of Fig. 2 indicates that the faces of the nanoassemblies for $n > 3$ are qualitatively close to equilateral triangles. Therefore, many of these nanoclusters can be classified as deltahedra. The nomenclatures of the polyhedra formed by the vesicles and corresponding polyhedra formed by the JNPs are found in Table 2.

Figure 3 (A) shows that for all considered values of n, the JNPs radial distribution function, $g(r)$, are highly peaked at the distance between first-nearest neighbour JNPs. For $n \geq 5$, $g(r)$ exhibits higher order peaks, which indicates the highly ordered nature of these nanoclusters. In the cases of $n = 3$ and 4, $g(r)$ has a single peak, as indicated by inset (a) of Fig. 3 (A), and their corresponding bond angle distributions (BAD), $P(\theta)$, are peaked at 60° (see Fig. 3 (B)). This implies that the geometries of the self-assembled 3- and 4-JNPs clusters must correspond to the equilateral triangle and regular tetrahedron, respectively.

In the case of 6 JNPs, Fig. 3 (A) shows that the ratio between the positions of the second and first peaks of the RDF, $r_{(1,3)}/r_{(1,2)} = 1.414 \approx \sqrt{2}$. Fig. 3 (B) shows that its corresponding BAD is peaked at 60°. Therefore, 6 JNPs self-assemble into a regular octahedron. Note that the two peaks of the RDF of the 6-JNPs cluster are much narrower than the peaks of the RDF of 6 uniform NPs shown in Fig. 1 (D). Likewise, 12 JNPs self-assemble into an icosahedron since the ratios of the peaks of its $g(r)$, $r_{(1,3)}/r_{(1,2)} = 1.62$ and $r_{(1,4)}/r_{(1,2)} = 1.90$, are respectively equal to those of the regular icosahedron, i.e. $(1+\sqrt{5})/2 \approx 1.618$ and $\sqrt{10+2\sqrt{5}}/2 \approx 1.902$. Furthermore, Fig. 3 (B) shows that the corresponding $P(\theta)$ is peaked at 60°.

By extrapolation, one expects that 8 NPs should also self-assemble into the Platonic solid cube and that the corresponding LV should be an octahedron. However, Fig. 2 indicates that 8 NPs

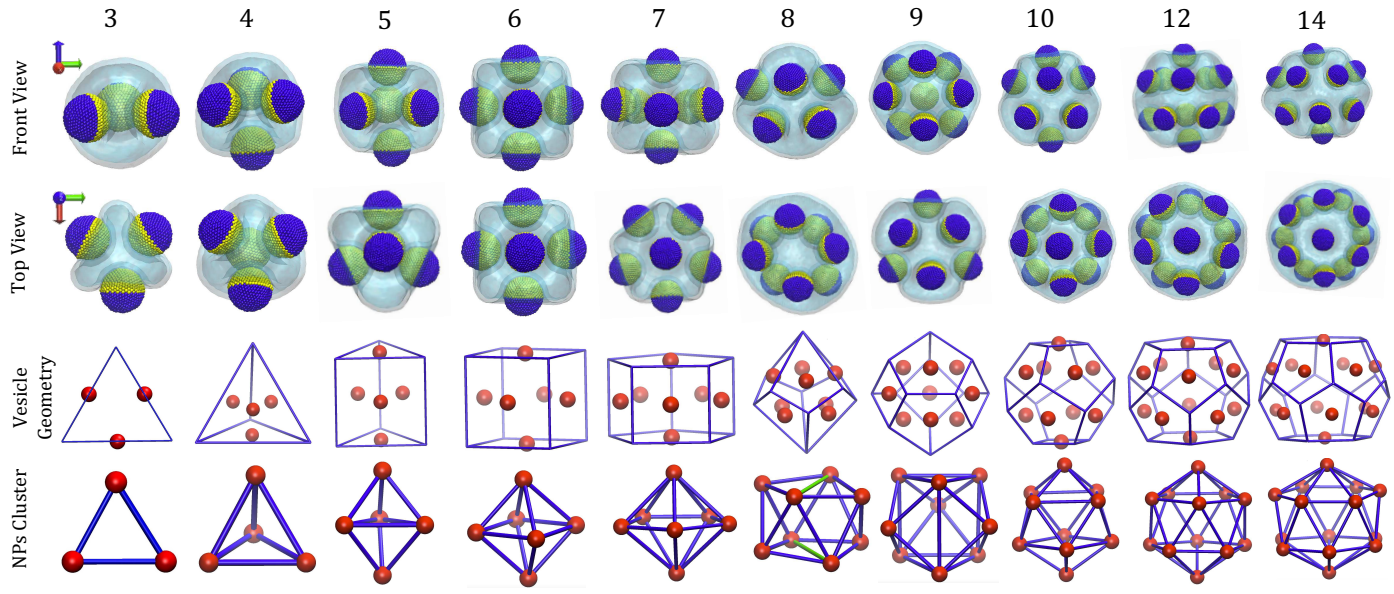

Fig. 2 First and second rows: Different snapshot views of LVs for $3 \leq n \leq 14$. The membrane is shown as icy blue. JNPs Moiety that interacts attractively (repulsively) with the LV is yellow (blue). Third row: Schematic geometries of the LVs. Blue lines correspond to highly bent regions of the LVs. Red beads represent the JNPs. Fourth row: Geometries of the JNP nanoclusters obtained from time averages of their positions at equilibrium. Vertices (red beads) correspond to the JNPs. Blue (green) segments are links between nearest neighbours JNPs obtained from Delaunay triangulation. Names of the LVs geometries and corresponding JNPs clusters are in Table 2. Simulations are performed on JNPs with $J = 0.5$ at $\xi = 4.11\,\mathrm{nm}^2/k_BT$.

self-assemble into a less symmetric nanolcuster with a geometry that is close to a square antiprism, and that the geometry of the corresponding LV is close to a tetragonal trapezohedron. The inability of 8 NPs to self-assemble into a cube, and the inability of the corresponding LV to form an octahedron, will be discussed later in detail.

We now turn our attention to the non-Platonic solid geometries formed by the LVs and the JNPs. Fig. 2 indicates that the geometry of the LV, in the case of $n = 5$ is a triangular prism, and that the corresponding NPs nanocluster is its dual, i.e. a triangular bipyramid. The RDF of the 5-NPs nanocluster exhibits 3 peaks with ratios $r_{(2,3)}/r_{(1,2)} \approx 1.11$ and $r_{(1,4)}/r_{(1,2)} \approx 1.51$. Fig. 3 (C) shows that the corresponding $P(\theta)$ exhibits two clear peaks at 55.5 and 69.0°, and a shoulder at 60.6°. Therefore, the geometry of the 5-NPs cluster is distorted from that of the triangular bipyramid deltahedron whose $g(r)$ has only two peaks at $r_{(1,2)}$ and $r_{(1,4)}$ (since $r_{(2,3)} = r_{(1,2)}$ for the triangular bipyramid deltahedron) with the ratio $r_{(1,4)}/r_{(1,2)} = 2\sqrt{2/3} \approx 1.63$, and its BAD has a single peak at 60°.

Similarly, the geometries of the nanoclusters for $n = 7$, 9 and 10, are also distorted from the pentagonal bipyramid deltahedron, triaugmented triangular prism deltahedron, and gyroelongated square bipyramid deltahedron, respectively. These distortions are demonstrated by the presence of more than one nearest-neighbour peaks in their respective $g(r)$ (see Fig. 3 (A)). Both 7- and 10-JNPs nanoclusters have two nearest-neighbour peaks with the ratio $r_{(2,3)}/r_{(1,2)} \approx 1.13$ and 1.14, respectively. The 9-NPs cluster has three nearest-neighbour peaks with ratios $r_{(2,3)}/r_{(1,2)} \approx 1.06$ and $r_{(3,4)}/r_{(1,2)} \approx 1.20$. These ratios should all be 1 if the nanocluster geometries were deltahedra. The distortion of the geometries from deltahedra is further demonstrated by their BAD, shown in Fig. 3 (C) for $n = 7$ and Fig. S5 (ESI†) for $n = 9$ and 10, which in the ideal case should have a single peak at 60°.

Table 2 Geometries of the vesicles and JNP nanoclusters for different values of n.

n	**Vesicle Geometry**	**NPs Nanocluster**
3	NA	equilateral triangle
4	regular tetrahedron	regular tetrahedron
5	triangular prism	triangular bipyramid
6	cube	regular octahedron
7	pentagonal prism	pentagonal bipyramid
8	quasi-tetragonal trapezohedron	quasi-square antiprism
9	order-4 truncated triangular bipyramid	triaugmented triangular prism
10	truncated square trapezohedron	gyroelongated square bipyramid
12	regular dodecahedron	regular icosahedron
14	truncated hexagonal trapezohedron	gyroelongated hexagonal bipyramid

Figure 2 shows that the 14-JNPs polyhedron corresponds to a gyroelongated hexagonal bipyramid. This geometry is contrasted with thus far discussed nanoclusters (with lower values of n), in that, a corresponding strictly convex 14-vertex deltahedron does

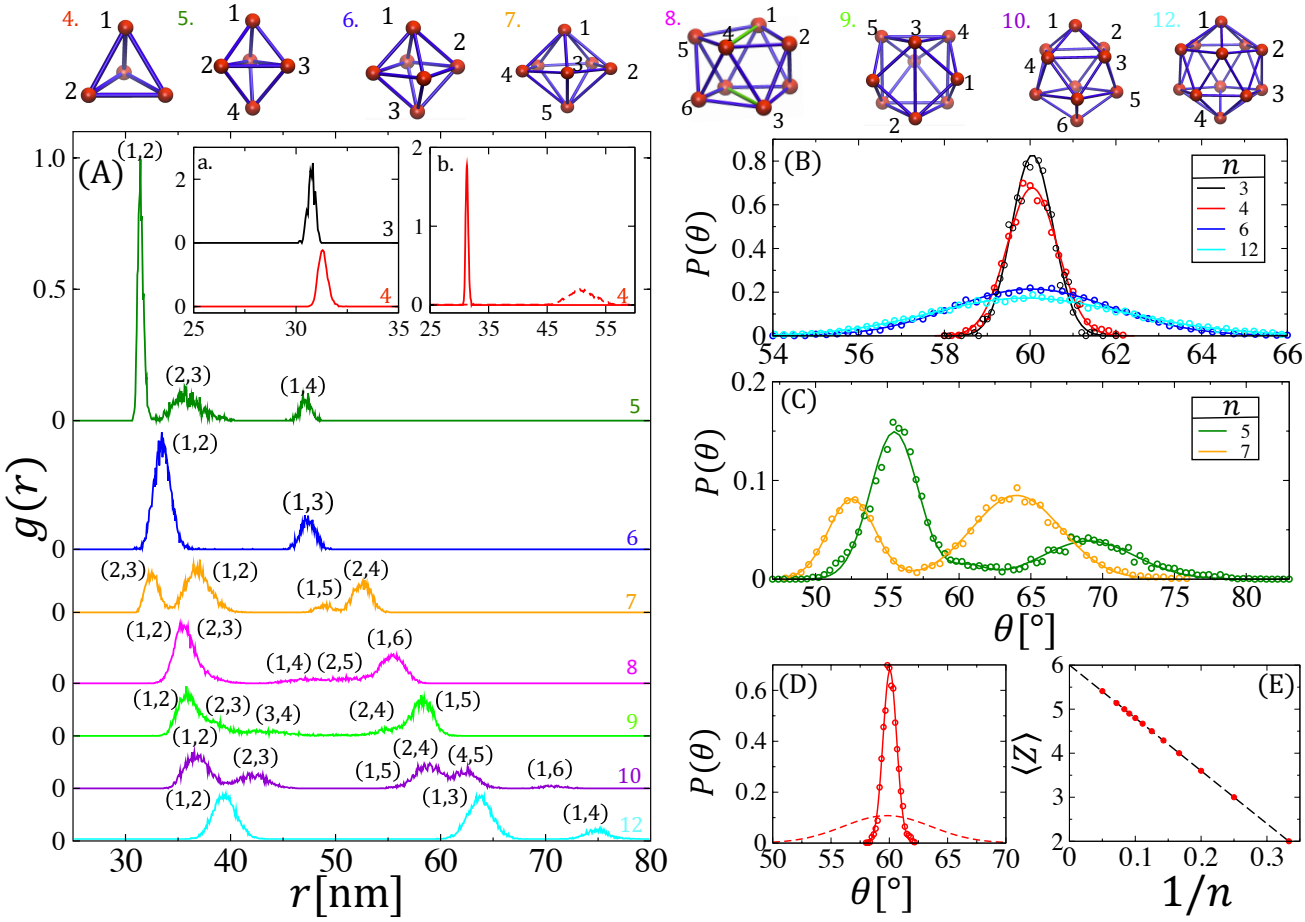

Fig. 3 (A) Radial distribution function, $g(r)$, for different values of n, on LVs with an area per JNP equal to 2453 nm^2. Inset (a): $g(r)$ for $n=3$ and 4. Inset (b): $g(r)$ for $n=4$ with $D_{ves}=56.2$ nm (solid line) and 96.2 nm (dashed line). (B) Bond angle distribution, $P(\theta)$, for $n=3$ and the three Platonic solids corresponding to $n=4$, 6 and 12. Solid lines are fits with Gaussians. (C) $P(\theta)$ for $n=5$ and 7. Green line is a fit with the sum of three Gaussians peaked at 55.5°, 60.6° and 69.0°. Orange line is a fit with two Gaussians peaked at 52.5° and 64.0°. (D) $P(\theta)$ for $n=4$ at $D_{LV}=56.2$ nm (solid line) and 96.2 nm (dashed line). (E) Average number of nearest neighbours per JNP vs $1/n$. The equation of the dashed line is $\langle Z\rangle = 6-12/n$. All results in this figure are based on simulations are performed on JNPs with $J=0.5$ at $\xi = 4.11\,\mathrm{nm}^2/k_BT$.

not exist. The corresponding $g(r)$ has 2 nearest neighbour peaks with a ratio very close to that of distorted deltahedra discussed above, i.e., $r_{(2,3)}/r_{(1,2)} \approx 1.10$. Likewise, 11 and 13 JNPs self-assemble into highly ordered structures, shown respectively in Figs. S6 and S7 (ESI†), although deltahedra with 11 or 13 vertices do not exist as well. ‘

We also inferred the stability of the structures by calculating the excess free energy, $\Delta F = \Delta F_{curv} + F_{adh}$, where F_{adh} is the net adhesion potential energy of the JNPs on the vesicle and $\Delta F_{curv} = F_{curv} - F_{curv}^{(0)}$ is the excess curvature energy of the vesicle ($F_{curv}^{(0)}$ and F_{curv} being the curvature energies of the bare vesicle and the vesicle with adhering JNPs, respectively). The curvature energy is calculated using an approach we introduced earlier based on the Helfrich Hamiltonian[46] in conjunction with a local Monge representation[31]. Details of this approach are found in Section SVI (ESI†). The obtained excess free energies, shown in Table S1 (ESI†), are negative. This agrees with the fact that the observed structures are stable. This table also shows that the free energy of a vesicle with n adhering JNPs is lower than the sum of the free energies of two smaller vesicles with n_1 and n_2 adhering JNPs, such as $n_1+n_2=n$. This implies that larger vesicles are more stable than smaller ones. However, this does not mean that two vesicles with adhered JNPs can spontaneously fuse to form a larger vesicle, since the fusion process of vesicles is associated with an energy barrier that is much larger than the thermal energy [47,48]. The energy barrier against the fusion of vesicles with adhering JNPs is expected to be even larger due to the repulsive interaction between the JNPs.

Figure 3 (E) shows that the average number of nearest neighbours of a JNP (coordination number $\langle Z\rangle$) agrees with the upper limit of Euler’s polyhedral formula (ULEPF) , i.e. $\langle Z\rangle = 6-12/n$[49]. Therefore, LVs self-assemble JNPs into polyhedra that maximize their coordination number. This relationship is particularly relevant to the case of 8 JNPs, which as discussed earlier, do not self-assemble into the Platonic solid cube, in contrast to the cases of $n=4$, 6 and 12. This is due to the fact that the coordination number of the cube, $Z=3$, is substantially lower than its corresponding ULEPF’s prediction, which is $Z=4.5$.

The results presented above, demonstrate that JNPs, with $4 \leq n \leq 10$ self-assemble into polyhedra that are either Platonic solids

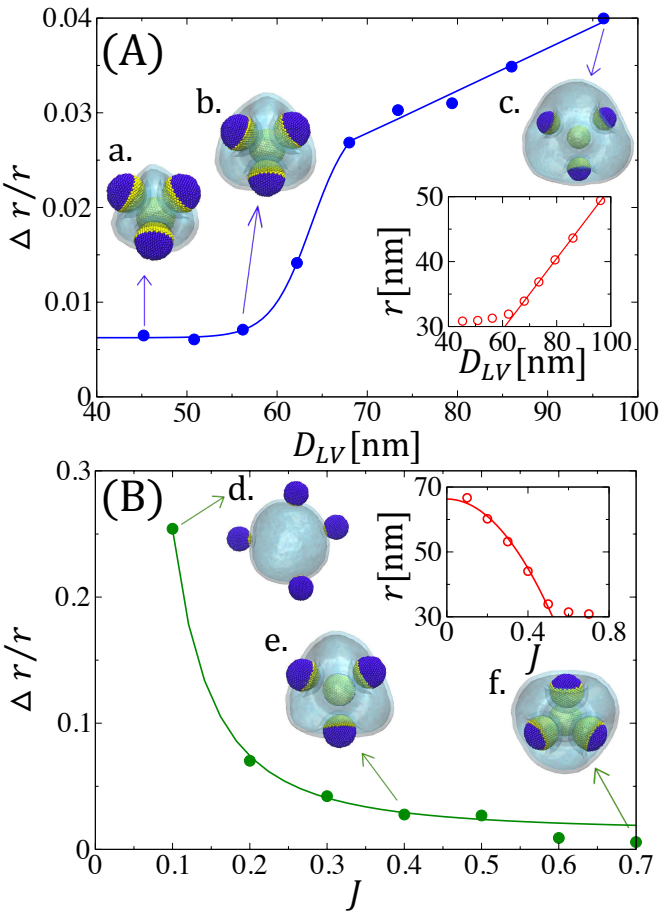

Fig. 4 (A) The deviation of the distance between NPs of the tetrahedron as a function of D_{LV} at $\xi = 4.11 k_B T/\text{nm}^2$ and $J = 0.5$. Inset of (A): Average distance between NPs as a function of D_{LV} at $\xi = 4.11 k_B T/\text{nm}^2$ and $J = 0.5$. (B) The deviation of the distance between NPs of the tetrahedron as a function of J at $\xi = 4.11 k_B T/\text{nm}^2$ and $D_{LV} = 68\,\text{nm}$. Inset of (B): Average distance between NPs as a function of J at $\xi = 4.11 k_B T/\text{nm}^2$ and $D_{LV} = 68\,\text{nm}$. Snapshots (a-f) are at equilibrium.

or slightly distorted deltahedra, except for $n = 8$, whose deltahedron is the snub-disphenoid[50], which is highly anisotropic. Interestingly, the degree of distortion of the nanoclusters geometries from their deltahedron counterparts, measured by $\Delta\theta = \sqrt{\langle(\theta - 60^\circ)^2\rangle}$ is highest in the case of $n = 8$ ($\Delta\theta \approx 10.5^\circ$) (see Table S2 (ESI†)). This high distortion is apparent in the bond angles of triplets $(2,1,4)$ and $(1,2,4)$ of cluster 8 in Fig. 3, which are respectively close to 45° and 90°, as indicated by Fig. S5 (ESI†). This results in the length of bond (1,4), shown by the green segment in Figs. 2 and 3, that is substantially higher than that of bond (1,2) or (2,3). Therefore, the JNPs polyhedron in the case of $n = 8$ must be closer to the square antiprism, which is not a deltahedron, than the snub-disphenoid.

Inset (b) of Fig. 3 (A) shows that the distance between the JNPs increases with the diameter of the vesicle. How does such a dilation affect the details of the JNP clusters and the fluctuations in the distance between the JNPs? To answer this question, we performed a series of simulations for different values of D_{LV} in the case of $n = 4$ and $J = 0.5$ at $\xi = 4.11 k_B T/\text{nm}^2$. The inset of Fig. 4 (A) shows that the distance between the JNPs, r, which corresponds to the location of the RDF's peak increases with increasing D_{LV} and that this increase is proportional to D_{LV} for $D_{LV} \gtrsim 60$ nm. This is due to the fact that the degree of wrapping of the JNPs by the membrane saturates at about $D_{LV} = 65$ nm. Therefore, further increase in the diameter of the LV, leads to an increase in the area of vesicle that is not in contact with the JNPs. Fig. 4 (A) shows that the relative fluctuations in r, i.e., $\Delta r/r$, increases with D_{LV}. However, the values of $\Delta r/r$ remain very small, which implies that the JNPs nanoclusters remain very ordered. This is clearly demonstrated by the snapshot (c) at $D_{LV} = 96.2$ nm. One expects that the nanoclusters should become disordered at large values of D_{LV}. We have therefore performed a large scale simulation for the case of $n = 4$ on a large vesicle with $D_{LV} = 142.4$ nm (see Fig. S8 (ESI†)), i.e. about 7 times the size of the JNPs. We found that even in this case, the peak of the RDF remains well defined, which demonstrates the robustness of the order of these nanoclusters. Determining the value of D_{LV} at which the nanoclusters become disordered would therefore require very long simulations on even larger vesicles, a task that is computationally very costly at the moment.

The saturation of r at low values of D_{LV} in the inset of Fig. 4 (A) is due to crowding of the confined JNPs on the LV, as shown by the snapshot (a,b) at $D_{LV} = 45.2$ nm and 56.2 nm in this figure. In the limit of small vesicles, the distance between the JNPs centers approach $D_{NP} + 2w \approx 28$ nm, where $w \approx 4$ nm is the width of the membrane in this model. This value is very close to the minimum value of r in the inset of Fig. 4 (A).

Likewise, we also investigated the effect of Janusity J on the order of the nanoclusters, through a series simulations for different values of J in the case of $n = 4$ and $D_{LV} = 68$ nm at $\xi = 4.11 k_B T/\text{nm}^2$. The inset of Fig. 4 (B) shows that the average distance between the JNPs decreases with J, which is simply due to the increase in the degree of wrapping of the JNPs with J, and therefore a decrease in the amount of LV's area that is not in contact with the JNPs. The decrease in $\Delta r/r$ with J, shown by Fig. 4 (B), implies an increase in the degree of order of the JNPs nanocluster with J until $J \approx 0.8$ where endocytosis occurs. This is also demonstrated by the RDFs at different values of J shown in Fig. S10 (ESI†). In particular, the relatively large values of $\Delta r/r$ for $J \lesssim 0.3$ implies that the effectiveness of LVs in self-assembling JNPs requires a fairly large degree of wrapping of the JNPs. This is in line with the results discussed earlier in the context of uniform NPs for relatively low values of ξ (see Fig. 1), which show that the NPs positions in the disordered phase are poorly correlated.

The stability of the numerically observed 8-JNPs nanostructure relative to the three other possible structures, i.e. cube, snub-disphenoid and square antiprism, is inferred from biased simulations to force the JNPs to adopt these three geometries. This is achieved by adding a three-body potential given by Eq. (3) between the central beads of the JNPs, with a bending stiffness taken to be $333 k_B T$. The preferred bond angle $\varphi_0 = 60$, 90 or 45° for the square antiprism, $\varphi_0 = 60^\circ$ for the snub-disphenoid, and $\varphi_0 = 90$ or 45° for the cube. Equilibrium configurations of the structures obtained from the biased simulations and their corresponding RDFs are shown in Fig. 5. From these simula-

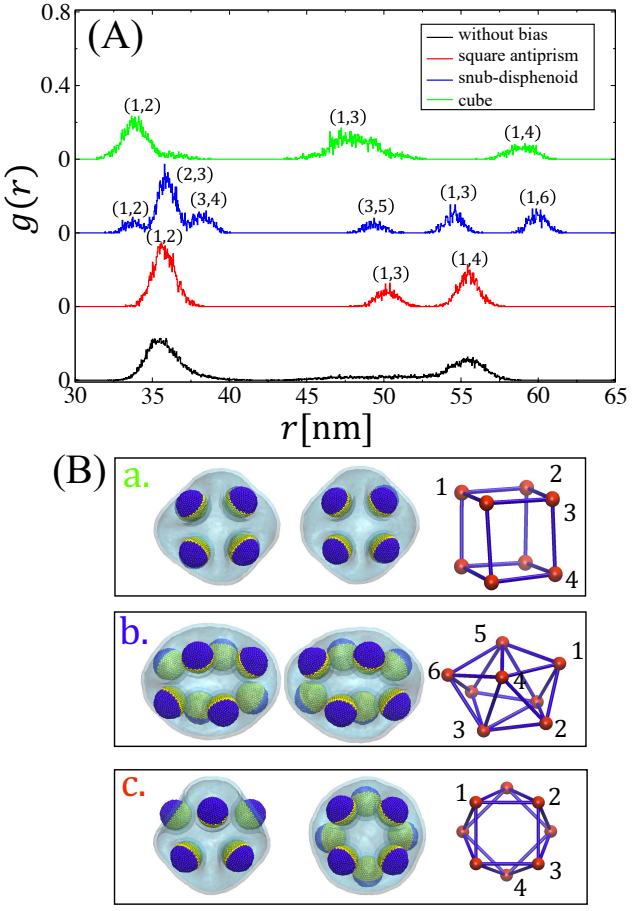

Fig. 5 (A) Radial distribution function of 8-JNPs clusters with different geometries. The green, blue and red curves are determined from biased simulations leading to geometries corresponding respectively to the cube, snub-disphenoid, square-antiprism. The black curve correspond to the unbiased system. (B) a, b and c show different views of the vesicles and and the nanoclusters formed by the JNPs obtained from the biased simulations. (a) corresponds to the cube, (b) corresponds to the snub-disphenoid and (c) corresponds to the square antiprism. In this figure, $J = 0.5$ and $\xi = 4.11\,\mathrm{nm}^2/k_BT$.

tions, we found that the average nearest neighbor distances are 33.90 nm for the cube, 35.96 nm for the snub disphenoid, and 35.75 nm for the square antiprism. The nearest neighbor distance of the unbiased structure is 35.62 nm, which is closest to that of square antiprism and snub-disphenoid. Based on nearest neighbor distance, the unbiased, square anti-prism and snub-disphenoid, should therefore be more favorable than the cube.

Since, for a given value of n, the net adhesion energy of the JNPs is found to be the same, regardless of the structure of the nanocluster, the relative stability of the different geometries, in the case of $n = 8$, is inferred from the excess curvature energy, $\Delta F_c = F_c - F_c^{(0)}$, of the LV in the four structures. Here $F_c(0)$ is the curvature energy of the bare vesicle with same size. The curvature energy is calculated using our approach based on the Helfrich Hamiltonian[46] in conjunction with a local Monge representation[31] (see Section SVI (ESI†) for details). The distributions of ΔF_c of the four structures, shown in Fig. 6 demonstrate that

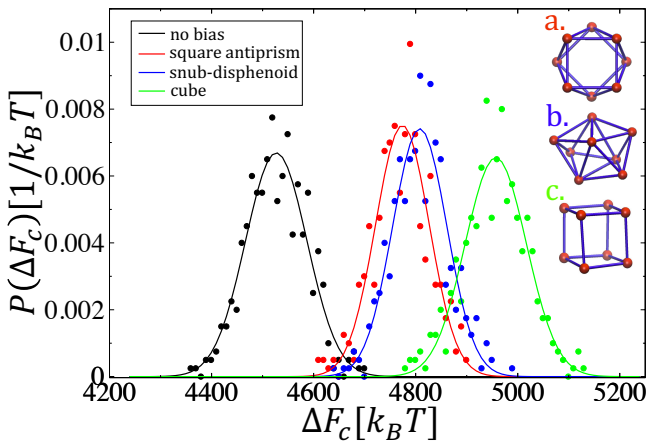

Fig. 6 Normalized distributions of the LVs excess curvature energy, ΔF_c, defined in the text, for $n = 8$. (a-c) correspond to the cases of an LV with JNPs adhering into an antiprism, snub-disphenoid and cubic nanocluster, respectively.

the unbiased structure is indeed most stable and that the cubic structure is least stable. Moreover, the curvature energy of the unbiased structure is closest to that of the square anti-prism. This must be due to the fact that the unbiased structure of 8-JNPs is closest to that of the square antiprism, as demonstrated by the snapshots in Fig. 2. This suggests that the vesicle, with adhering JNPs, adopts a shape with minimum curvature energy, and this happens to be a vesicle shape that maximizes the coordination number of the JNPs nanocluster polyhedron. We believe that this is due to a curvature induced repulsive interaction between the JNPs.

The relatively high curvature energy of the snub-disphenoid (see Fig. 6) must be due to its high anisotropy (see snapshots (b) in Fig. 6), although this structure satisfies ULEPF ($Z = 4.5$). The reason why the snub-disphenoid geometry of the JNPs nanocluster is not selected must be due to the fact that the snub-disphenoid is fairly elongated, and therefore the vesicle corresponding to this nanocluster must have highly curved regions.

To further validate our finding that LVs self-assemble spherical JNPs into polyhedra which maximize Z, we performed a simulation of 20 JNPs and found that they do not self-assemble into a dodecahedron, which does not satisfy ULEPF ($Z = 3$ for the dodecahedron). Instead, 20 JNPs self-assemble into a structure shown in Fig. S11 (ESI†), which satisfies ULEPF ($\langle Z \rangle = 5.4$). As n and D_{LV} are further increased, the vesicle polyhedra become more spherical, and the JNPs form mostly a triangular lattice on the LV, with about 12 JNPs having 5 nearest neighbours. For example, this is shown by the snapshot obtained from a large simulation of 32 JNPs on a vesicle with $D_{LV} = 158$ nm (see Fig. S12 (ESI†)). This implies that in the limit of planar membranes, i.e., for $D_{LV} \to \infty$, the JNPs are expected to self-assemble into a triangular lattice.

4 Conclusion

We demonstrated, in this article, that LVs are able to self-assemble spherical Janus NPs into highly ordered nanoclusters, which cannot be achieved in the case of spherical NPs with uniform sur-

faces. The conditions allowing for these self-assemblies are a Janusity less than about 0.8 and a high enough adhesion strength to induce full wrapping of the moieties of the JNPs which interact attractively with the lipid head groups, while preventing their endocytosis. In these LVs-induced ordered nanoclusters, the JNPs are apart from each other, with a distance between nearest neighbour JNPs determined by their number on the LV and the size of the LV. The geometry of these nanoclusters is determined by the number of the JNPs. We found that for a given value of n, the specific polyhedron of the JNPs is selected such that the upper limit of Euler's polyhedral formula is achieved. As a result, 4, 6 and 12 JNPs self-assemble into the platonic solids corresponding to the regular tetrahedron, octahedron, and icosahedron. In contrast, 8 and 20 JNPs do not form the Platonic solids corresponding to the cube and dodecahedron since these do not satisfy the ULEPF.

Systematic simulations over varying values of the LV's diameter and JNPs' Janusity show that the degree of order of these nanoclusters decreases with increasing D_{LV}. However, it increases with J. Nevertheless, the nanoclusters remain fairly ordered even when the distance between nearest neighbour JNPs is as large as about 100 nm.

The results presented in this article are very exciting in that they demonstrate that lipid vesicles have the potential to be used as an alternative medium for self-assembling Janus NPs into highly ordered nanoclusters. Although challenging, experimental studies are warranted to validate our results.

Conflicts of interest

There are no conflicts of interest to declare.

Acknowledgements

This work was supported by a grant from the National Science Foundation (DMR-1931837). The simulations were performed on computers of the High Performance Computing Facility at the University of Memphis. Portions of the computational aspects of this research were conducted as part of a user project at the Center for Nanophase Materials Sciences (CNMS), which is a US Department of Energy, Office of Science User Facility at Oak Ridge National Laboratory. This research used resources of the Oak Ridge Leadership Computing Facility, which is a DOE Office of Science User Facility supported under Contract DE-AC05-00OR22725. Snapshots in this article were generated using VMD version 1.9.3 [51].

Notes and references

1 S. Singamaneni, V. N. Bliznyuk, C. Binek and E. Y. Tsymbal, *J. Mater. Chem.*, 2011, **21**, 16819–16845.

2 S. Kundu and A. Patra, *Chem. Rev.*, 2017, **117**, 712–757.

3 J.-M. Lamarre, F. Billard, C. H. Kerboua, M. Lequime, S. Roorda and L. Martinu, *Opt. Comm.*, 2008, **281**, 331–340.

4 C. Yu, X. Guo, M. Shen, B. Shen, M. Muzzio, Z. Yin, Q. Li, Z. Xi, J. Li, C. T. Seto and S. Sun, *Ang. Chem. Int. Ed.*, 2018, **57**, 451–455.

5 X. Wu, C. Hao, J. Kumar, H. Kuang, N. A. Kotov, L. M. Liz-Marzán and C. Xu, *Chem. Soc. Rev.*, 2018, **47**, 4677–4696.

6 S.-Y. Ding, E.-M. You, Z.-Q. Tian and M. Moskovits, *Chem. Soc. Rev.*, 2017, **46**, 4042–4076.

7 G. P. Acuna, F. M. Möller, P. Holzmeister, S. Beater, B. Lalkens and P. Tinnefeld, *Science*, 2012, **338**, 506–510.

8 *Anal. Chem.*, 2010, **82**, 9058–9065.

9 S. S. Aćimović, M. P. Kreuzer, M. U. González and R. Quidant, *ACS Nano*, 2009, **3**, 1231–1237.

10 S. Cui, S. Zhang and S. Yue, *J. Healthc. Eng.*, 2018, **2018**, 1–11.

11 L. Yang, J. Wei, Z. Ma, P. Song, J. Ma, Y. Zhao, Z. Huang, M. Zhang, F. Yang and X. Wang, *Nanomaterials*, 2019, **9**, 1789.

12 M. S. M. Saifullah, M. Asbahi, D. C. J. Neo, Z. Mahfoud, H. R. Tan, S. T. Ha, N. Dwivedi, T. Dutta, S. bin Dolmanan, Z. Aabdin, M. Bosman, R. Ganesan, S. Tripathy, D. G. Hasko and S. Valiyaveettil, *Nano Lett.*, 2022, **22**, 7432–7440.

13 H. Kang, F. m. c. A. Detcheverry, A. N. Mangham, M. P. Stoykovich, K. C. Daoulas, R. J. Hamers, M. Müller, J. J. de Pablo and P. F. Nealey, *Phys. Rev. Lett.*, 2008, **100**, 148303.

14 C. A. Mirkin, R. L. Letsinger, R. C. Mucic and J. J. Storhoff, *Nature*, 1996, **382**, 607–609.

15 R. Veneziano, S. Ratanalert, K. Zhang, F. Zhang, H. Yan, W. Chiu and M. Bathe, *Science*, 1986, **352**, aaf15.

16 M. Stevens, N. Flynn, C. Wang, D. Tirrell and R. Langer, *Adv. Mat.*, 2004, **16**, 915–918.

17 K. L. Gurunatha, A. C. Fournier, A. Urvoas, M. Valerio-Lepiniec, V. Marchi, P. Minard and E. Dujardin, *ACS Nano*, 2016, **10**, 3176–3185.

18 H. Tian and J. He, *Langmuir*, 2016, **32**, 12269–12282.

19 P. Kühler, E.-M. Roller, R. Schreiber, T. Liedl, T. Lohmüller and J. Feldmann, *Nano Lett.*, 2014, **14**, 2914–2919.

20 E.-M. Roller, L. V. Besteiro, C. Pupp, L. K. Khorashad, A. O. Govorov and T. Liedl, *Nature Phys.*, 2017, **13**, 761–765.

21 M. Pilo-Pais, A. Watson, S. Demers, T. H. LaBean and G. Finkelstein, *Nano Lett.*, 2014, **14**, 2099–2104.

22 K. Matsuura, G. Ueno and S. Fujita, *Polym. J.*, 2015, **47**, 146–151.

23 L. Xu, W. Yan, W. Ma, H. Kuang, X. Wu, L. Liu, Y. Zhao, L. Wang and C. Xu, *Adv. Mat.*, 2015, **27**, 1706–1711.

24 M. J. Urban, P. K. Dutta, P. Wang, X. Duan, X. Shen, B. Ding, Y. Ke and N. Liu, *J. Am. Chem. Soc.*, 2016, **138**, 5495–5498.

25 W. Chen, A. Bian, A. Agarwal, L. Liu, H. Shen, L. Wang, C. Xu and N. A. Kotov, *Nano Lett.*, 2009, **9**, 2153–2159.

26 I. Koltover, J. O. Rädler and C. R. Safinya, *Phys. Rev. Lett.*, 1999, **82**, 1991–1994.

27 K. Sugikawa, T. Kadota, K. Yasuhara and A. Ikeda, *Ang. Chem. Int. Ed.*, 2016, 4059–4063.

28 C. van der Wel, A. Vahid, A. Šarić, T. Idema, D. Heinrich and D. J. Kraft, *Sci. Rep.*, 2016, **6**, 32825.

29 A. Šarić and A. Cacciuto, *Phys. Rev. Lett.*, 2012, **109**, 188101.

30 A. H. Bahrami, R. Lipowsky and T. R. Weikl, *Phys. Rev. Lett.*, 2012, **109**, 188102.

31 E. J. Spangler, P. B. Sunil Kumar and M. Laradji, *Soft Matter*, 2018, **14**, 5019–5030.

32 E. J. Spangler and M. Laradji, *J. Chem. Phys.*, 2021, **154**, 244902.

33 A. Sharma, Y. Zhu, E. J. Spangler, J.-M. Y. Carrillo and M. Laradji, *Soft Matter*, 2023, –.

34 C. Kaewsaneha, P. Tangboriboonrat, D. Polpanich, M. Eissa and A. Elaissari, *ACS Appl. Mat. Int.*, 2013, **5**, 1857–1869.

35 B. J. Reynwar, G. Illya, V. A. Harmandaris, M. M. Müller, K. Kremer and M. Deserno, *Nature*, 2007, **447**, 461–464.

36 A. H. Bahrami and T. R. Weikl, *Nano Lett.*, 2018, **18**, 1259–1263.

37 Y. Zhu, A. Sharma, E. J. Spangler and M. Laradji, *Soft Matter*, 2022, **18**, 4689–4698.

38 J. D. Revalee, M. Laradji and P. B. Sunil Kumar, *J. Chem. Phys.*, 2008, **128**, 035102.

39 M. Laradji, P. B. Sunil Kumar and E. J. Spangler, *J. Phys. D: Appl. Phys.*, 2016, **49**, 293001.

40 J. R. Baumgardner and P. O. Frederickson, *SIAM J. Num. Anal.*, 1985, **22**, 1107–1115.

41 G. S. Grest and K. Kremer, *Phys. Rev. A*, 1986, **33**, 3628–3631.

42 J. F. Nagle, M. S. Jablin, S. Tristram-Nagle and K. Akabori, *Chem. Phys. Lipids*, 2015, **185**, 3–10.

43 W. C. Swope, H. C. Andersen, P. H. Berens and K. R. Wilson, *The Journal of Chemical Physics*, 1982, **76**, 637–649.

44 A. Sharma, Y. Zhu, E. J. Spangler and M. Laradji, *J. Chem. Phys.*, 2022, **156**, 234901.

45 M. Caroli, P. M. M. de Castro, S. Loriot, O. Rouiller, M. Teillaud and C. Wormser, Experimental Algorithms, Berlin, Heidelberg, 2010, pp. 462–473.

46 W. Helfrich, *Z. Naturforsch. C*, 1973, **28**, 693–703.

47 J. Lee and M. Schick, *Biophysical Journal*, 2008, **94**, 1699–1706.

48 A. Grafmüller, J. Shillcock and R. Lipowsky, *Biophysical Journal*, 2009, **96**, 2658–2675.

49 D. S. Richeson, *Euler's Gem: The Polyhedron Formula and the Birth of Topology*, Princeton University Press, 2008.

50 N. W. Johnson, *Canad. J. Math.*, 1966, **18**, 169–200.

51 W. Humphrey, A. Dalke and K. Schulten, *J. Mol. Graph.*, 1996, **14**, 33–38.